Journal of Solid State Electrochemistry (2019) 23:1861–1870
https://doi.org/10.1007/s10008-019-04283-9

ORIGINAL PAPER

Inexpensive methodology for obtaining flexible SnO_2-single-walled carbon nanotube composites for lithium-ion battery anodes

Fábio R. Bento[1] · Patricia G. Corradini[1] · Lucia H. Mascaro[1]

Received: 3 February 2019 / Revised: 22 April 2019 / Accepted: 23 April 2019 / Published online: 11 May 2019

Abstract

A versatile and low-cost methodology for fabricating free-standing carbon graphite (CG)/SnO_2/single-walled carbon nanotube (SWCNT) composites as anode material for lithium-ion batteries is described. CG–SnO_2 (1:1) was ball milled and the composite obtained was dispersed with different ratios (wt%) of SWCNT. Then, the flexible composite CG–SnO_2–SWCNT was successfully manufactured by a simple vacuum filtration procedure. Electrochemical measurements demonstrated that the anode composite paper with 50 wt% CG–SnO_2 and 50 wt% SWCNT showed excellent retention of a high specific capacity (318 mA h g^{-1}) after 30 cycles at current density of 0.08 mA cm^{-2}, which was twice that of SWCNT paper (155 mA h g^{-1}). This SWCNT–CG–SnO_2 combination is very promising, since the SWCNT could act as a flexible mechanical support, while CG–SnO_2 provides high capacity. This paper presents an inexpensive methodology that may be applied to the design of electrodes and evaluates the interaction between SnO_2 and carbon materials as anode in lithium-ion battery systems.

Keywords Single-walled carbon nanotubes · Tin oxide · Lithium-ion batteries

Introduction

Lithium-ion batteries (LIBs) have been widely investigated because of their high-energy density, long cycle life and high efficiency [1, 2]. Because of these qualities, this technology has increased in commercial use by powering portable electronic devices and electric vehicles. LIBs consist of a negative electrode, usually of graphite (theoretical capacity of 372 mA h g^{-1}); a positive electrode, commonly using a lithium intercalation compound (e.g., $LiCoO_2$ or $LiMn_2O_4$); and an electrolyte, which allows the flow of lithium ions between the electrodes [3, 4]. In LIB technology, the anode plays a crucial role in the electrochemical performance of the battery. One of the challenges in LIBs is to improve the capacity and cycling life of their anode materials. Thus, the physical and chemical properties of anode materials must be considered and controlled appropriately.

Since 1938 carbon graphite (CG) has been suggested for rechargeable battery applications; in 1977, this material was considered as a good candidate for lithium-intercalated systems. Due to its low cost, superior chemical resistance and cycling stability, graphite remain as the main anode support material in commercial Li-ion batteries and it has been extensively reviewed ever since [5]. Current, other structured carbon-based materials, such as carbon nanotubes (CNTs), have been highlighted, especially for storage of electrochemical energy due to their particular morphology, structure and physical and chemical proprieties [6–9]. As an anode material for LIBs, CNTs show good cycling stability, but a large and irreversible capacity loss in the first cycle. Chew et al. [9] reported a comparative study of free-standing electrodes made from three different types of commercial CNTs: single-walled (SWCNT), double-walled (DWCNT) and multi-walled (MWCNTs). The experiments showed that films based on MWCNTs exhibited a reversible charge of approximately 300 mA h g^{-1} with a stable cycling behaviour, whereas SWCNT and DWCNT films showed strong fading. For these reasons, the intercalation capacity of Li ions in carbonaceous material is still limited.

More recently, CG–MO (carbon graphite–metal oxide) compounds have become an interesting class for anode material, showing theoretical capacities two to three times higher than graphite [10]. As an example, tin dioxide (SnO_2) has been intensely investigated as anode material for LIBs due

✉ Lucia H. Mascaro
lmascaro@ufscar.br

[1] Department of Chemistry, Federal University of São Carlos, Rod. Washington Luiz, Km 235, São Carlos, SP 13565-905, Brazil

to a high theoretical capacity of 781 mA h g^{-1}, low cost, high abundance and low toxicity [11]. However, volume expansion of this electrode material during the repeated insertion and extraction of Li ions causes electrode spraying and loss of electrical contact, leading to a rapid capacity fade [11]. To overcome these problems, various strategies have been applied to improve the electrochemical performance of SnO_2-based anodes. One effective strategy is to incorporate SnO_2 into a carbon-based material. SnO_2-based carbon composites have been shown to be good candidates for LIB anodes [12–17]. This behaviour is due to that the carbon, being a flexible and conductive matrix, can not only limit the volume expansion of SnO_2 but can also enhance the electrical conductivity of the integral material, resulting in improved electrochemical performance. For example, Qin et al. [15] developed novel interconnected sandwiched carbon-coated hollow nanostructures (C@SnO_2@C) which exhibited a long-life high-rate cycling stability for LIB anodes. Guo et al. [16] reported SnO_2 nanoparticles uniformly coated onto graphene nanosheets (GNs). The SnO_2-graphene composite showed a high reversible capacity, good cycling and excellent high-rate discharge performance; superior electrochemical properties were compared to pure graphene [16]. Likewise, Wang et al. proposed SnO_2-carbon nanotube–graphene nanosheet (SnO_2–CNT–GN) as anode material for LIBs [17]. They commented that the addition of CNTs increases the connection of relatively independent graphene sheets, delivering faster charge–transfer pathways at the SnO_2 interface and better mechanical properties and flexibility. Therefore, a SnO_2–CNT–GN electrode exhibits higher reversible capacity and rate capability than does a SnO_2–GN electrode.

The demand for different battery designs has increased the development of new wearable and flexible materials [18]. To address flexible materials for LIBs, free-standing electrodes have stood out in recent years, aiming at elimination of the stiff components used in manufacturing of active materials for LIBs, such as current collectors and polymeric binders. In particular, Ng et al. [19] have reported a flexible electrode composed of SWCNT. The free-standing SWCNT paper electrode was synthesised by a simple filtration method using positive pressure. The authors commented that the electrode is lightweight, flexible and has good conductivity and is described as a promising material for lithium-ion battery anodes [19].

In this paper, composites of CG, SnO_2 and SWCNT were fabricated applying a filtration method using positive pressure. The composite paper electrodes do not require metallic current collectors or polymeric binders because the composite paper itself serves as both the active material and the current collector. In addition, the influence of the wt% of C–SnO_2 composite added to prepared paper electrodes on the electrochemical performance of all-solid-state LIBs was investigated.

Experimental section

Preparation of CG–SnO_2 and [CG–SnO_2]$_x$–SWCNT$_{(1-x)}$ composite papers

The fabrication process of free-standing [CG–SnO_2]$_x$–SWCNT$_{(1-x)}$ composite paper is illustrated in Fig. 1. The CG–SnO_2 composite was prepared by ball-milling. Carbon graphite (Sigma-Aldrich®) and SnO_2 (Nanostructured & Amorphous Materials Inc.®, 99.5%) were mixed (CG/SnO_2 mass ratio = 1:1). The CG–SnO_2 powder was ball milled in a planetary ball mill (Fristcn GmbH®) in a

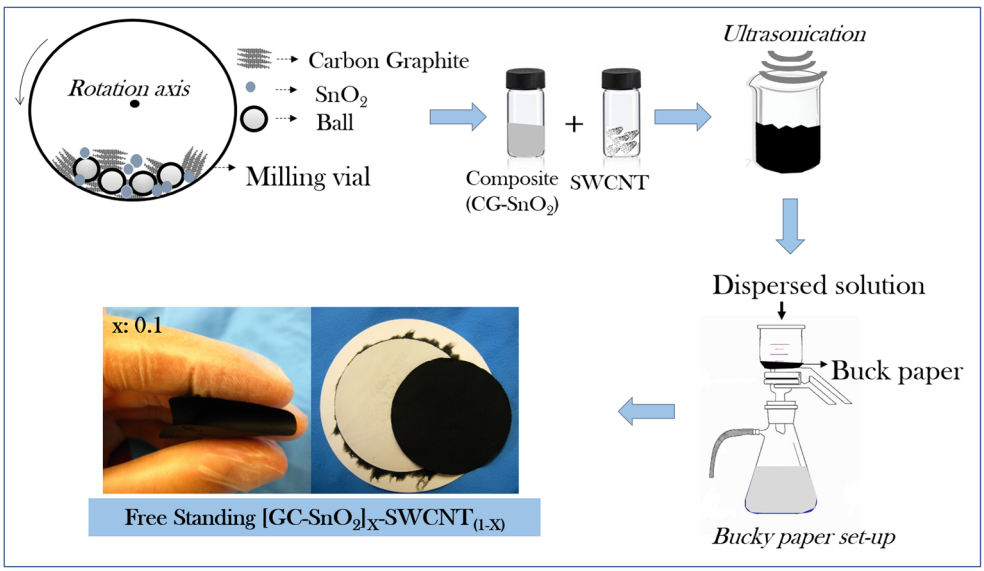

Fig. 1 Illustrative scheme for the production of [C–SnO_2]$_x$–SWCNT$_{(1-x)}$ composite paper electrodes

stainless steel vessel at 140 rpm for 6 h. The ball/powder weight ratio was 20:1.

A series of [CG–SnO_2]–SWCNT mixtures, with SWCNT (Carbon Nanotechnologies Incorporated®, USA, carbon > 95%, lot P0323) content 50, 70, 90 and 100 wt%, were prepared. A dispersion was prepared of 30 mg of $[CG–SnO_2]_x–SWCNT_{(1-x)}$ ($x = 0$, 0.1, 0.3, and 0.5) and 1.0 g of surfactant (Triton X-100, Sigma-Aldrich®) into 80 mL of ultra-pure water, followed by ultra-sonication for 6 h.

The next step was prepared the free-standing $[CG–SnO_2]_x–SWCNT_{(1-x)}$ ($0 \le x \le 0.5$) composite paper using simple filtration method via positive pressure (Fig. 1). The as-prepared suspension was filtered through a porous polyvinylidene fluoride (PVDF) membrane (Millipore®, 0.22 μm pore size, 47 mm diameter). The membrane acts as a filter, and the membrane was wetted with ultra-pure water and ethanol solution (50:50 *v*/*v*) for 30 min. The as-prepared $[CG–SnO_2]_x–SWCNT_{(1-x)}$ suspensions were filtered by wetted PVDF membrane in a filtration cell under positive nitrogen gas pressure of 400 kPa. Then, the resultant $[CG–SnO_2]_x–SWCNT_{(1-x)}$ was washed with 200 mL of ultra-pure water followed by 100 mL of methanol. Finally, the $[CG–SnO_2]_x–SWCNT_{(1-x)}$ was peeled from PVDF filter after drying overnight in a vacuum oven.

The $[CG–SnO_2]_{0.1}–SWCNT_{0.9}$ composite paper exhibited good flexibility, as seen at Fig. 1. However, this flexibility is affect by the increasing of wt% of the C–SnO_2. For example, it was observed that the composite paper containing higher than 50 wt% of SWCNT and 50 wt% of C–SnO_2 ($[CG–SnO_2]_{0.5}–SWCNT_{0.5}$) was cracked.

Material characterisation

The X-ray diffraction (XRD) spectra of $[CG–SnO_2]_x–SWCNT_{(1-x)}$ composite papers were recorded on a Siemens AXS Analytics D5005 X-ray diffractometer (CuKα = 0.15406 nm, 40 kV and 30 mA). The scan rate was 1° min^{-1}. Scanning electron microscopy (SEM) images were realised by high-resolution field emission gun–scanning electron microscopy (FEG–SEM) (Supra 35-VP, Carl Zeiss, Germany). For the composition mapping, a Philips XL-30 FEG microscope coupled to an energy-dispersive X-ray spectroscopy (EDX) detector was used. A Horiba iHR 550 micro-Raman spectrophotometer was used to obtain room-temperature Raman spectra. The laser source was 544 nm for all samples. X-ray photoelectron spectroscopy (XPS) measurements were carried out on Scienta Omicron (model ESCA 2SR) spectrometer. The incident photon energy was provided by magnesium monochromator (Mg Kα), calibrated using the carbon 1s peak (284.8 eV).

Electrochemical measurements

The prepared $[CG–SnO_2]_x–SWCNT_{(1-x)}$ composite papers were cut to 0.5 cm × 0.5 cm and used as electrodes for LIBs with no current collector. Electrochemical measurements were carried out by using two-electrode coin cells. CR 2032 coin-type cells were assembled in an argon-filled glovebox (Mbraun, Unilab®) with $[CG–SnO_2]_x–SWCNT_{(1-x)}$ composite paper as the working electrode and Li foil as the counter electrode. The electrolyte was 1.0 mol L^{-1} $LiPF_6$ in a mixture of ethylene carbonate (EC, Merck®) and dimethyl carbonate (DMC, Merck®) of 1:1 *v*/*v*. The Li-ion insertion/extraction behaviours of $[CG–SnO_2]_x–SWCNT_{(1-x)}$ binder-free films were investigated by cyclic voltammetry (CV) and galvanostatic charging/discharging tests between 0.01 and 2.0 V (vs. Li/Li^+) at a current density of 0.08 mA cm^{-2}.

CV measurements were performed on a CHI 660 A electrochemical workstation at scanning rate of 0.1 mV s^{-1}. Electrochemical impedance spectroscopy (EIS) measurements were also carried out on CHI 660A electrochemical workstation, at an AC voltage of 10 mV amplitude in the frequency range 100 kHz–10 mHz.

Results and discussion

Physical characterisation of $[CG–SnO_2]_x–SWCNT_{(1-x)}$

Figure 2a presents XRD spectra for the SWCNT and the $[CG–SnO_2]_x–SWCNT_{(1-x)}$ ($x = 0$, 0.1, 0.3 and 0.5 wt%). Pure SWCNT showed three peaks, at approximately 37°, 43.3° and 63.7°. No graphite form (~ 25.6°) was observed, which indicated a high degree of crystallinity of the SWCNT [20, 21]. Some authors have indexed the 2θ near 43.3° as the (101) plane of the SWCNT [20–22]. As this was the most intense peak in the spectra, there are probably some preferential crystallographic orientations of SWCNT [22]. For all $[CG–SnO_2]_x–SWCNT_{(1-x)}$ proportions, the crystalline form for SnO_2 is cassiterite (JCPDS 72-1174—data in Fig. 2a, inset) [20]. By the Scherrer equation, the estimated average crystallite size of SnO_2 for $[CG–SnO_2]_x–SWCNT_{(1-x)}$ of all proportions was 23.2 ± 0.4 nm, and of carbon, it was 40.8 ± 0.1 nm.

Raman spectra of SWCNT and of $[CG–SnO_2]_x–SWCNT_{(1-x)}$ of all proportions are represented in Fig. 2b. The peak highlight as D_{peak} (~ 1325 cm^{-1}) corresponds to the breathing mode of sp^2 atoms in a ring, reflecting the disorder and/or defects at the hexagonal graphitic layer. G_{peak} is related to bond stretching of all pairs of sp^2 atoms in a two-dimensional hexagonal lattice (ring or chain) [14, 21, 23]. For SWCNT, a typical G_{peak} is split into at least two components: at 1520 and 1578 cm^{-1}, named G^- and

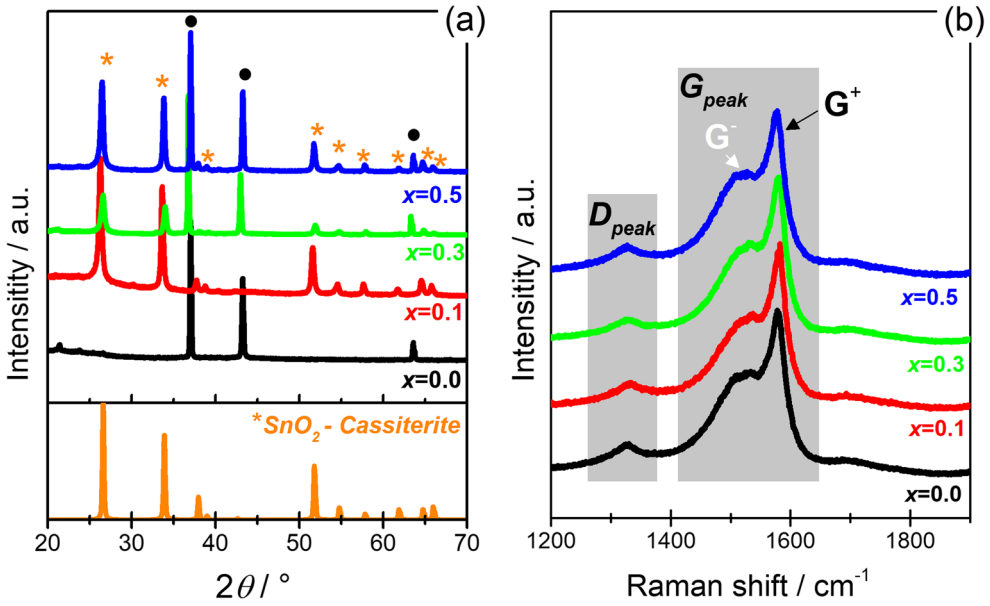

Fig. 2 **a** XRD spectra and **b** micro-Raman spectra of $[CG–SnO_2]_x–SWCNT_{(1–x)}$ composite paper electrodes

G^+, respectively [24–27]. The spacing between G^+ and G^- is proportional to the diameter of the nanotubes and suggests high electrical conductivity [26]. As the Raman profiles are very similar, it is possible to infer that the addition of SnO_2 does not change the SWCNT structure.

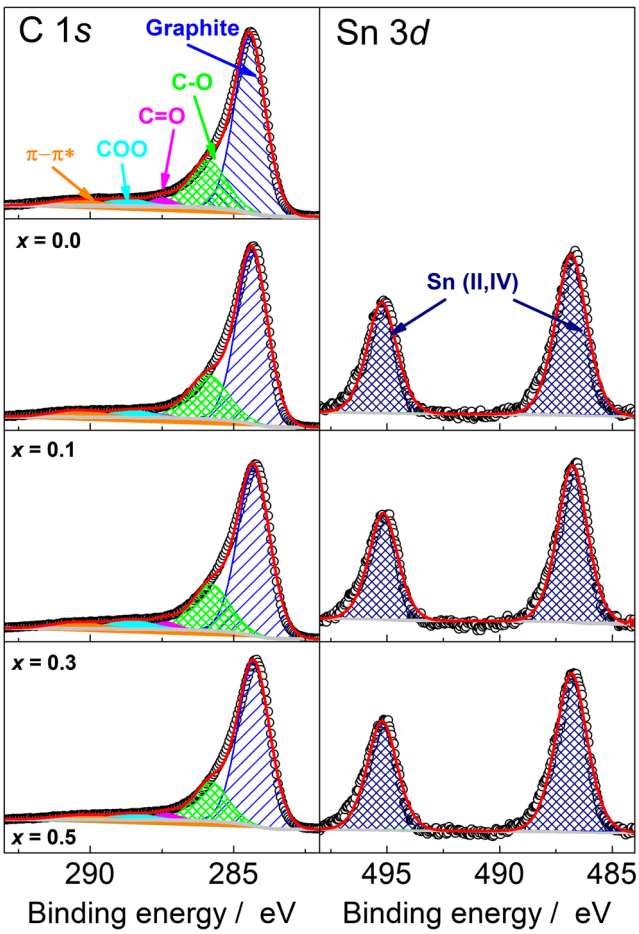

Fig. 3 C 1*s* and Sn 3*d* XPS spectra for $[CG–SnO_2]_x–SWCNT_{(1–x)}$ composite paper electrodes

Figure 3 represents the XPS spectra in the binding energy regions related to the C 1*s* and Sn 3*d* orbitals of the $[CG–SnO_2]_x–SWCNT_{(1–x)}$ composite paper electrodes. The spectra of C 1s were deconvoluted in five signals, which correspond to different binding states observed between the carbons typically common in SWNCT. The most intense peak was in 284.4, named as graphite, which refers to C=C and C–C bonds [23, 28]. The peak at 285.9 eV is correlated to C–O interaction of phenolic hydroxyl groups [3]. Other three with low contributions are related to cetone/quinone (C=O), carboxyl groups (COO) and aromatic interaction (π–π*), at 287.5 eV, 288.7 eV and 290.5 eV respectively [23]. For Sn 3*d* spectra, only a peak was observed in all composition: Sn (II, IV) around 487.1 eV [29, 30], confirming that the tin presents only in oxidised form. The separation between the Sn^{2+} and Sn^{4+} assignments is difficult due the overlapping of the bonding energies of these forms, but probably the form present in these materials is SnO_2, which is the most stable structure [29]. The preparation of the electrodes did not affect the carbon and tin structure, since there were no major differences in the XPS spectra.

The microstructure and morphology of the free-standing electrodes were observed by SEM, as show in Fig. 4. As shown in Fig. 4a, and observed in all SWCNT composites, the tube network was composed of continuous SWCNT, which were result of tube self-assembly by van der Waals force during filtration [31]. After addition of C–SnO_2, the microstructure of the SWCNT was well maintained and the surface consisted

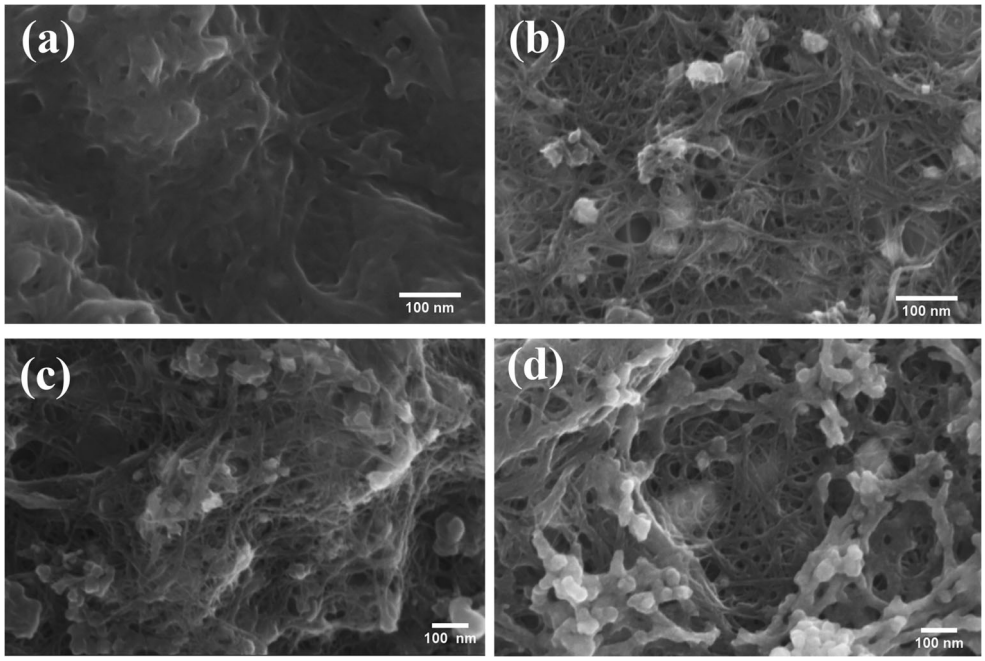

Fig. 4 SEM images for $[CG–SnO_2]_x–SWCNT_{(1-x)}$ composite paper electrodes. **a** $x = 0.0$. **b** $x = 0.1$. **c** $x = 0.3$. **d** $x = 0.5$

of numerous SnO_2 particles, Fig. 4b–d. In Fig. 4d, the FEG–SEM images of $[CG–SnO_2]_{0.5}–SWCNT_{0.5}$ show a structure with many irregular carbon hollows supporting agglomerations of SnO_2 particles. These change the specific area, electrical resistance and diffusion characteristics and therefore can alter the energy storage and rate capacity of the prepared electrodes. Therefore, $[CG–SnO_2]_{0.5}–SWCNT_{0.5}$ may be able to promote adsorption of the electrolyte into the electrode and enhance the transportation of Li ions over the entire electrode.

Figure 5 presents a sequence of images to illustrate better the different dimensions of the $[CG–SnO_2]_{0.5}–SWCNT_{0.5}$ electrode. Figure 5a shows the diameter size of the paper electrode, approximately 3 cm. Figure 5b shows the FEG–SEM image of the

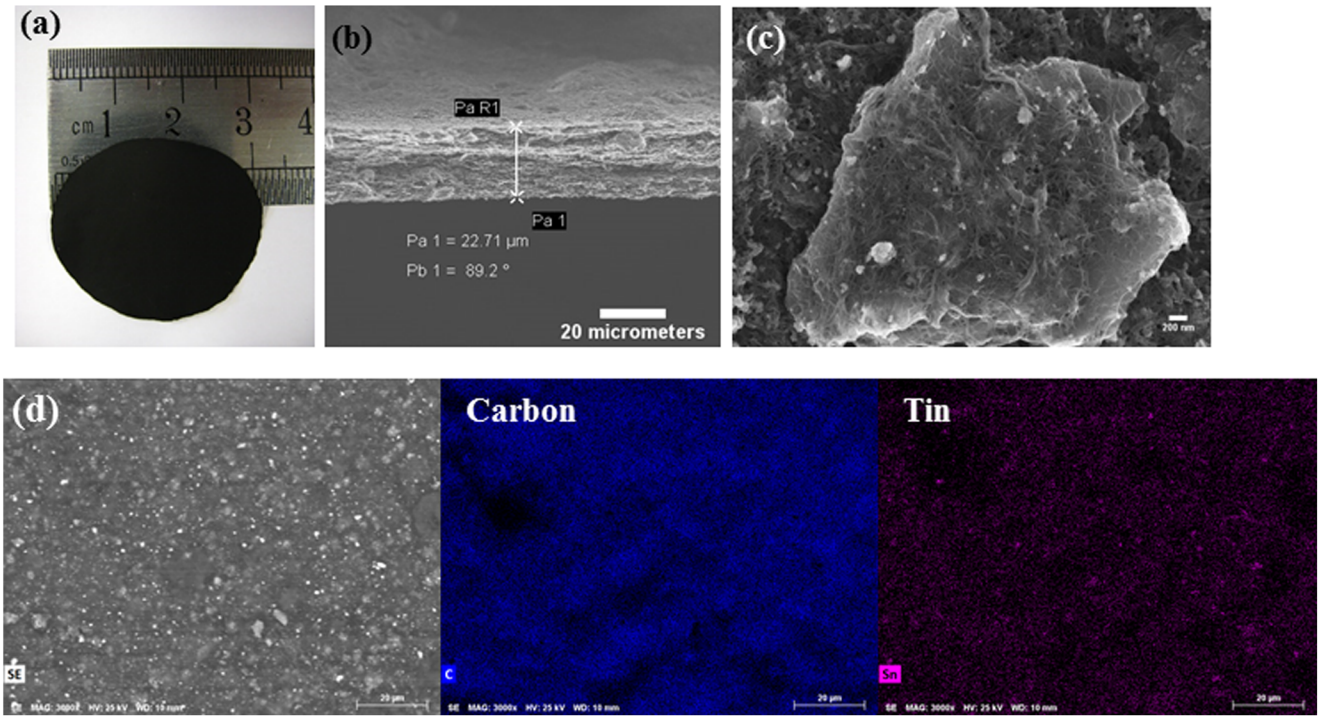

Fig. 5 **a** Photograph of paper electrode. **b** Cross-sectional FEG-SEM and **c** SEM image of the for $[CG–SnO_2]_{0.5}–SWCNT_{0.5}$. **d** EDX elemental mapping was carried out for $[CG–SnO_2]_{0.5}–SWCNT_{0.5}$, for carbon and tin spatial distribution

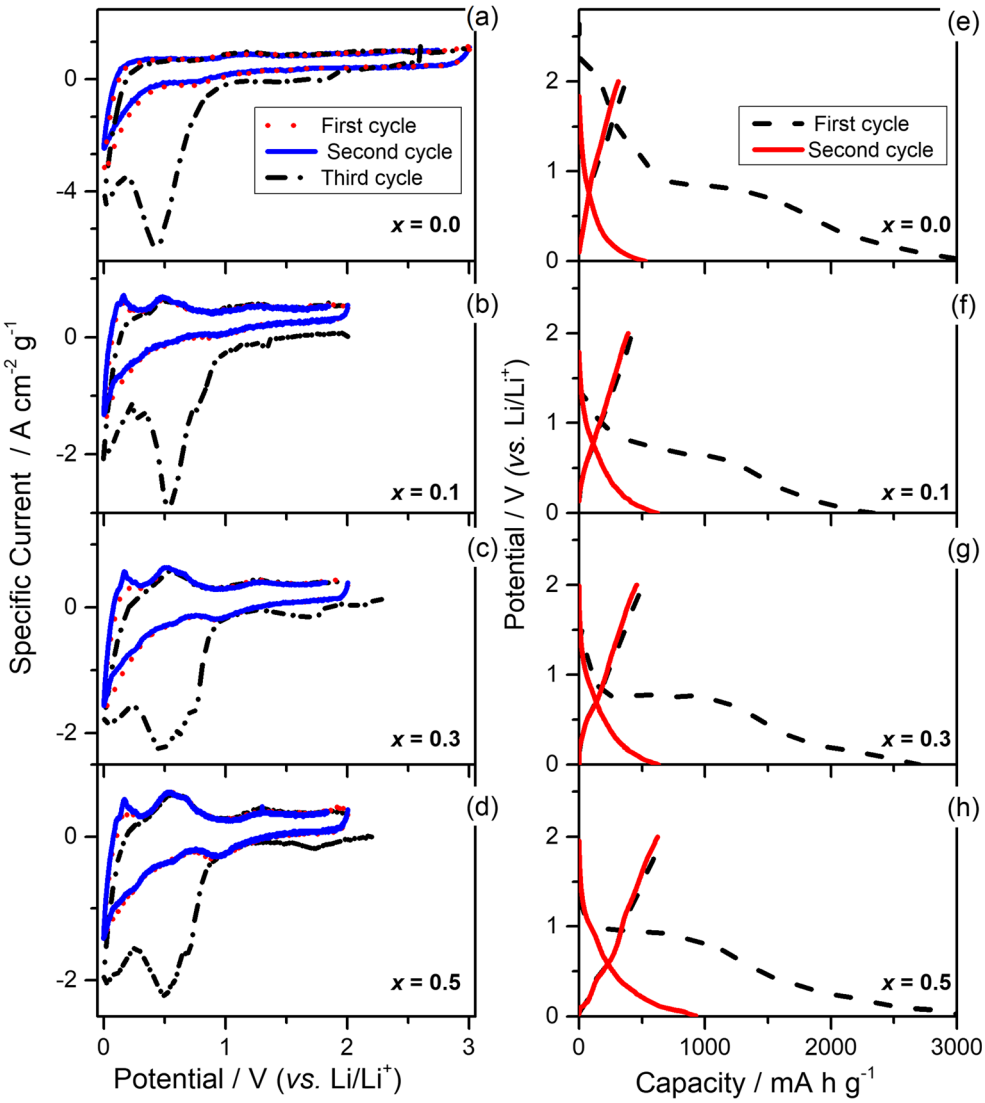

Fig. 6 Cyclic voltammograms at the first three cycles of $[CG–SnO_2]_x–SWCNT_{(1–x)}$ composite paper electrodes at 0.1 mV s^{-1} of **a** $x = 0.0$, **b** $x = 0.1$, **c** $x = 0.3$, and **d** $x = 0.5$. Charge/discharge profiles at 0.08 mA h g^{-1} of $[CG–SnO_2]_x–SWCNT_{(1–x)}$ composite paper electrodes: **e** $x = 0.0$, **f** $x = 0.1$, **g** $x = 0.3$, and **h** $x = 0.5$

cross-sectional of $[CG–SnO_2]_{0.5}–SWCNT_{0.5}$, which formed the thickest film of ≅ 23 μm. The SWCNT electrodes showed a dense packing, encouraging the use of this simple methodology for the manufacture of electrodes. The composite has a well defined and interconnected three-dimensional porous network, as observed in Fig. 5c. It can be observed that the SWCNT cover the CG surface and, at the same time, intra-pores would be created to increase the specific area, making the Li ions more accessible to the electrode surface. In order to confirm the homogenous SnO_2 particle distribution, FEG–SEM and disperse spectrum (EDS) analyses were also performed of the top view of $[CG–SnO_2]_{0.5}–SWCNT_{0.5}$ of the free-standing electrodes. As shown in Fig. 5d, EDX elemental mapping was carried out for $[CG–SnO_2]_{0.5}–SWCNT_{0.5}$ to verify the spatial distribution of Sn and C. The mapping images indicated that the carbon (CG and SWCNT) and Sn elements were evenly distributed. The area mapping clearly shows that the composite electrode consists predominantly of carbon.

Electrochemical properties

Figure 6a–d shows the CV curves of $[CG–SnO_2]_x–SWCNT_{(1–x)}$ electrodes ball milled with different wt% of $CG–SnO_2$, in three cycles at a scan rate of 0.1 mV s^{-1}. The shape of CV curves obtained for the cells in this study is in accordance with similar CV plots found in the literature [15, 19, 32]. During the first cycle, there are a serie of reduction peaks, which can be attributed to various reactions, as presented below. Moreover, the first Li insertion curve is significantly different from the subsequent ones. During the first cathodic sweep, the broad reduction peak located at around 0.55 V, which disappears entirely in the following cycles, can be attributed to the formation of a solid electrolyte interphase (SEI) layer on the electrode surface as a result of electrolyte decomposition, Eq. 1 [12]:

$$Li^+ + e^- + \text{electrolyte} \rightarrow \text{SEI (Li)} \quad (1)$$

The interactions with Li^+, SnO_2 and carbonaceous species can be described by Eqs. 2–4 [12]:

$$4\,Li^+ + SnO_2 + 4e^- \rightarrow Sn + 2Li_2O \quad (2)$$

$$xLi^+ + Sn + xe^- \leftrightarrows Li_xSn\ (0 \le x \le 4.4) \quad (3)$$

$$yLi^+ + C + ye^- \leftrightarrows Li_yC \quad (4)$$

The $[CG–SnO_2]_{0.0}$–$SWCNT_{1.0}$ electrode exhibits a broader SEI formation peak, as seen in Fig. 6a. This peak indicates that the kinetics of the SEI formation is favoured in carbon-based material [33]. Lithium can intercalate reversibly between the carbon nanotube channels [34]. However, no well-defined redox potential peak for lithium insertion can be identified from CV measurements. For $[CG–SnO_2]_x$–$SWCNT_{(1-x)}$ ($0.1 \le x \le 0.5$), in Fig. 6b–d, the cathodic peak located at 0.55 V can be ascribed to the reduction of SnO_2 to Sn^0 and the formation of an SEI, as in Eqs. (2) and (1), respectively. The other peak, ranging from 0.40 to 0.01 V, is attributed to the reversible formation of Li_xSn alloys ($0.0 \le x \le 4.4$; Eq. (3)) and insertion of Li ions into the channels between nanotubes, Eq. (4) [35, 36]. This behaviour shows that CG–SnO_2 was well dispersed in the SWCNT matrix, and probably, all materials were active during the first cycle. In the subsequent anodic scan, the CV curves keep fairly stable and almost overlap with each other, implying a good cycling stability of the $[CG–SnO_2]_x$–$SWCNT_{(1-x)}$ composite paper electrodes ball milled with different wt% of CG–SnO_2. With addition of CG–SnO_2, three other peaks, at 0.16 V, 0.60 V and 1.30 V, are observed, corresponding to the decomposition of Li_xSn alloys, the oxidation of Sn^0 to SnO or SnO_2 and lithium extraction from vacancies in the ball-milled graphite, respectively [37]. It was possible to see the large potential hysteresis due to Li-ion in inserted near 0.0 V and removal at about 1.30 V vs. Li/Li^+. This result is very similar to those reported in literature [34, 38, 39]. Figure 6e–h presents the galvanostatic charging/discharging curves of cells containing $[CG–SnO_2]_x$–$SWCNT_{(1-x)}$ electrodes with varying C–SnO_2/SWCNT ratios between 2.0 and 0.01 V (vs. Li/Li^+) in the initial cycles at a current density of 0.08 mA cm^{-2}. In all cases, there is a large an irreversible loss in capacity after the first cycle, owing to the decomposition of electrolyte and the formation of an SEI layer. The charging process of $[CG–SnO_2]_x$–$SWCNT_{(1-x)}$ composite paper can be divided into three main stages: (i) a potential declining at 2.00–0.80 V; (ii) a large pseudo-plateau at about 0.80 V, which can be related to SEI film formation and Sn metal formation in the Li_2O matrix; and (iii) 0.50–0.01 V region, corresponding to intercalation of Li ions in carbonaceous materials and Li–Sn alloy formation. The results were consistent with the voltage plateaus in the CV curves. Moreover, apart from the first discharge profile, the following discharge and charge profiles coincide with each other, exhibiting good reversible electrochemical properties and satisfactory structural stability for $[CG–SnO_2]_x$–$SWCNT_{(1-x)}$ composite paper.

Table 1 shows the specific charge and discharge capacities and coulombic efficiency at the first, second and 30th cycles. $[CG–SnO_2]_{0.0}$–$SWCNT_{1.0}$ anode indicates the lowest capacity compared to $[CG–SnO_2]_x$–$SWCNT_{(1-x)}$ ($0.1 \le x \le 0.5$) composite paper electrodes for the first and second cycles. The initial charge/discharge capacity and the initial coulombic efficiency were 3133/374 mA h g^{-1} and 11.96%, for $[CG–SnO_2]_{0.0}$–$SWCNT_{1.0}$, respectively. The discharge capacity and coulombic efficiency all increased as the C–SnO_2 ratio in the SWCNT paper electrodes increased. The sample with highest content of C–SnO_2 (50 wt%) achieved the highest discharge capacity in the first cycle, of 673 mA h g^{-1} and a coulombic efficiency of 21.83%. For the second cycle, the reversible capacity of the $[CG–SnO_2]_{0.0}$–$SWCNT_{1.0}$ electrode was 311 mA h g^{-1}, whereas for $[CG–SnO_2]_{0.5}$–$SWCNT_{0.5}$, it was 623 mA h g^{-1}, almost twice as high. These results not only demonstrate that the SWCNT acts as an active material for lithium storage and a flexible film in the $[CG–SnO_2]_x$–$SWCNT_{(1-x)}$ materials but also confirm the synergistic effect between the C–SnO_2 particles and the SWCNT. The results demonstrated that the SWCNT contributed to the larger initial irreversible capacity. This higher consumption of energy should be relative to the reduction of dioxygen molecules or oxygenated functional groups present in SWCNT [40]. After 30 cycles, $[CG–SnO_2]_{0.0}$–$SWCNT_{1.0}$ showed a specific capacity of 155 mA h g^{-1} which is only 49% of the reversible capacity after the second cycle (311 mA h g^{-1}). Thus, for the second cycle, the sample $[CG–SnO_2]_{0.0}$–$SWCNT_{1.0}$ provided almost the theoretical capacity of carbonaceous materials if we assume that one Li ion interacts with six atoms of carbon, which could deliver 372 mA h g^{-1}.

Table 1 Specific capacities and coulombic efficiency of $[CG–SnO_2]_x$–$SWCNT_{(1-x)}$ composite paper electrodes with varying C–SnO_2 ratios at first, second and 30th cycles

$[CG–SnO_2]_x$–$SWCNT_{(1-x)}$	Charge capacity (mA h g^{-1})			Discharge capacity (mA h g^{-1})			Coulombic efficiency (%)		
	First	Second	30th	First	Second	30th	First	Second	30th
0.0	3133	526	158	374	311	155	11.96	59.24	98.10
0.1	2334	621	232	424	389	213	18.18	62.65	91.81
0.3	2516	629	245	508	456	209	20.20	72.57	85.30
0.5	3081	926	361	673	623	311	21.83	67.30	86.15

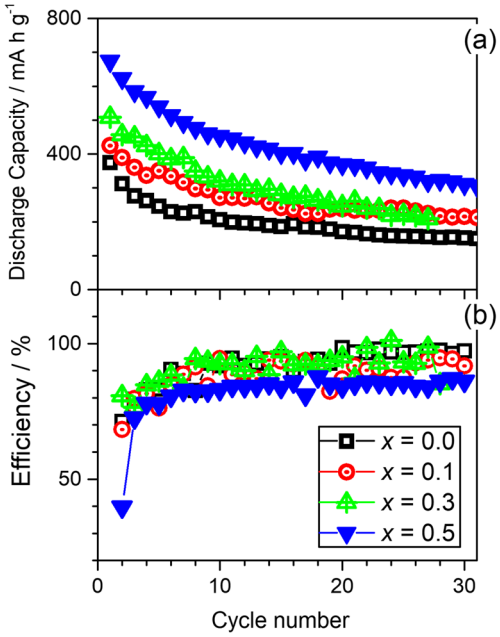

Fig. 7 **a** Reversible capacity and **b** energy storage efficiency *vs.* cycle number for 0.08 mA cm^{-2} of $[CG–SnO_2]_x–SWCNT_{(1–x)}$ $(0.0 \le x \le 0.5)$ composite paper

Probably, the continuous cycling decreased the retention of Li ions in the carbon structure. This loss of retention of Li ions is probably related to amorphous carbon present and/or some defects on the nanotube walls [41]. On the other hand, even the addition of CG–SnO_2 was enough to stop the capacity loss in the battery during electrochemical cycling. The explanation for this behaviour is due to volume changes of SnO_2 caused by stress-induced material during the insertion/extraction of Li ions during cycling [11, 36]. But it can be seen that the reversible capacity is maintained above 311 mAh g^{-1} beyond 30 cycles for $[CG–SnO_2]_{0.5}–SWCNT_{0.5}$. We attribute the higher capacity observed for $[CG–SnO_2]_{0.5}–SWCNT_{0.5}$ to the synergistic interaction of GC–SnO_2 and Li ions in the composite.

The discharge capacity performance of $[CG–SnO_2]_x–SWCNT_{(1–x)}$ $(0.0 \le x \le 0.5)$ electrodes at a current density of 0.08 mA cm^{-2} is shown in Fig. 7a. The capacity of $[CG–SnO_2]_x–SWCNT_{(1–x)}$ ($x = 0.1$, 0.3 and 0.5) composites was higher than the pure SWCNT paper electrode. The addition of C–SnO_2 helped Li-ion intercalation. Notably, the reversible capacity of the $[CG–SnO_2]_{0.5}–SWCNT_{0.5}$ electrode was higher than that of the others. The energy storage efficiencies of $[CG–SnO_2]_x–SWCNT_{(1–x)}$ composite paper, where $0.0 \le x \le 0.5$, are summarised in Fig. 7b. The results indicate that $[CG–SnO_2]_{0.0}–SWCNT_{1.0}$ showed the highest energy storage efficiency of 98.1% in comparison to $[CG–SnO_2]_{0.1}–SWCNT_{0.9}$ (91.8%), $[CG–SnO_2]_{0.3}–SWCNT_{0.7}$ (95.3%) and $[CG–SnO_2]_{0.5}–SWCNT_{0.5}$ (86.2%) cells for the first 30 cycles. It was found that the SWCNT contributed to higher energy storage efficiencies. SWCNT materials present some advantages over CG–SnO_2 because there is no contribution of SnO_2 volume change to

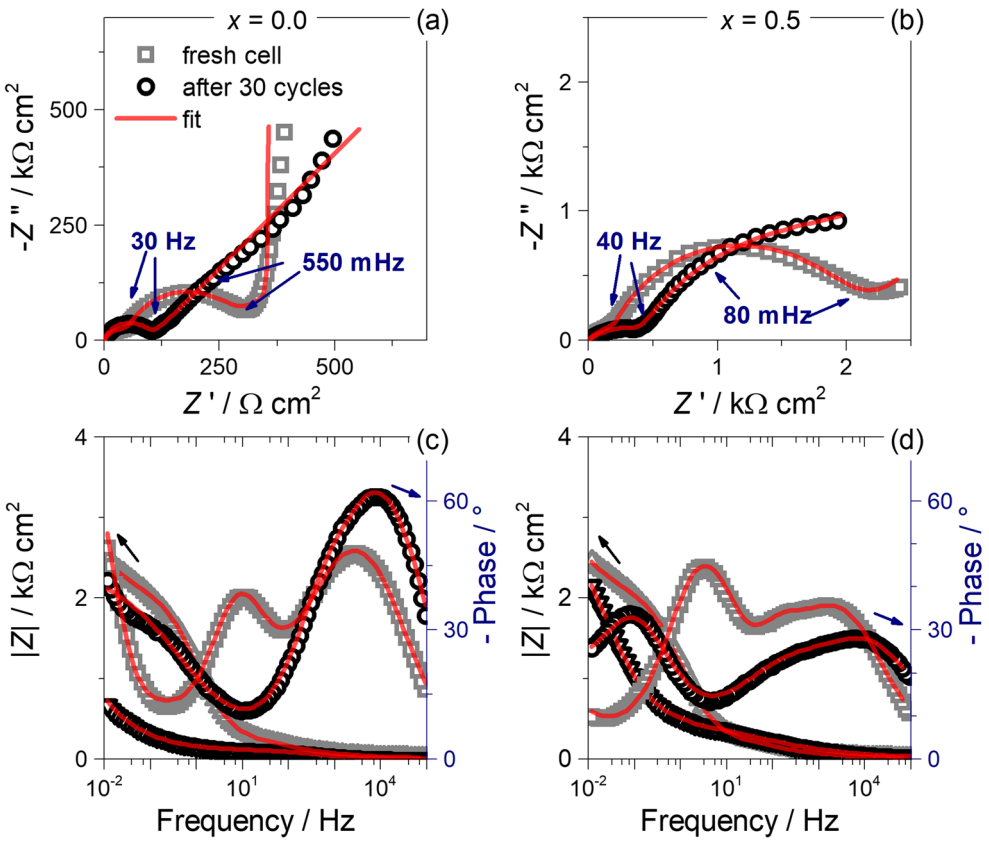

Fig. 8 Nyquist plots of **a** $[CG–SnO_2]_{0.0}–SWCNT_{1.0}$ paper electrode and **b** $[CG–SnO_2]_{0.5}–SWCNT_{0.5}$ composite paper electrode, at initial condition and after 30 cycles of charge/discharge. Bode plots of **c** $[CG–SnO_2]_{0.0}–SWCNT_{1.0}$ paper electrode and **d** $[CG–SnO_2]_{0.5}–SWCNT_{0.5}$ at initial condition and after 30 cycles of charge/discharge

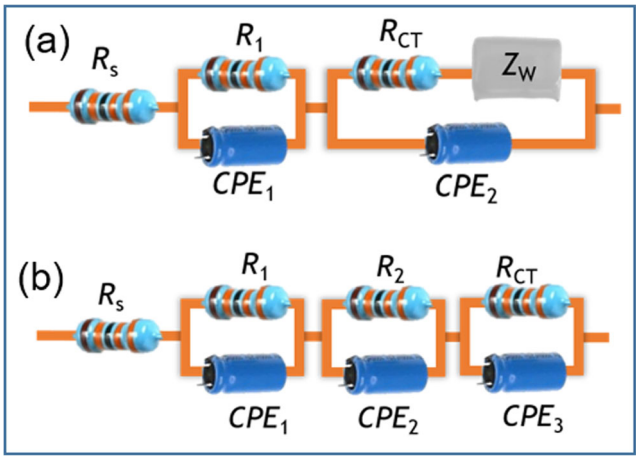

Fig. 9 Representation of equivalent circuit for EIS measures of **a** [CG–SnO_2]$_{0.0}$–$SWCNT_{1.0}$ and **b** [CG–SnO_2]$_{0.5}$–$SWCNT_{0.5}$ composite paper electrode

electrode efficiency during the charge–discharge process. However, even with 50 wt% addition of C–SnO_2, it is possible to see a good cycling stability and energy efficiency in CG–MO compounds.

EIS measurements were carried out to investigate the interface reactions between the electrolyte solution and the electrode and to investigate the effect of wt% of ball-milled CG–SnO_2 on variations in the charge–transfer resistance in [CG–SnO_2]$_x$–$SWCNT_{(1-x)}$ composite paper. Impedance tests were carried out on freshly assembled cells and after the cells had been cycled 30 times for $x = 0.0$ and 0.5, as showed in Fig. 8. The initial Nyquist and after 30 cycles diagrams for [CG–SnO_2]$_{0.0}$–$SWCNT_{1.0}$ (Fig. 8a) can be adjusted in two half circles: at the 100 kHz–250 Hz frequency (high frequency range) and the second half circle in the 254–550 Hz (mid frequency range). At Bode plot (Fig. 8c), it is possible to observe the change of impedance modulus and phase angle, which gives an idea of the components of system. In the high-frequency region, the semicircle is related to the electrolyte interface impedance (R_S), which is characterised by the electrolyte solution. The depressed semicircles at high and medium frequencies are associated with Li-ion migration and the charge–transfer process resistance (R_1 and R_{CT}) and pseudo-capacitance (CPE_1 and CPE_2). The straight line in the low-frequency region is credited to the Warburg behaviour (Z_W), and it is associated the Li-ion diffusion process within the electrodes. The equivalent circuit for [CG–SnO_2]$_{0.0}$–$SWCNT_{1.0}$ is illustrated at Fig. 9a. At Table 2, the R_S and R_{CT} are listed at fresh cell and after 30 cycles. R_S did not present significant value changes, indicating that the electrolyte showed no degradation for the tests. The R_{CT} decreasing indicated that the Li-ion electrons can transfer more freely in the electrode/electrolyte interface after cycling for [CG–SnO_2]$_{0.0}$–$SWCNT_{1.0}$.

A different response was obtained for the fresh [CG–SnO_2]$_{0.5}$–$SWCNT_{0.5}$ electrode, Fig. 8b. In this case, the impedance response corresponding to the diffusion process was not observed. The impedance to the fresh cell and after 30 cycles can be distributed in three processes, since three half-circles can be adjusted. The Bode plots (Fig. 8d) shows that between 100 and 10,000 Hz, two shoulders are observed at phase angle, indicating that two processes occur in near time. However, one more resistance and pseudo-capacity can be observed, probably related to the addition of SWCNT. Figure 9b presents the equivalent circuit for [CG–SnO_2]$_{0.5}$–$SWCNT_{0.5}$ electrode. For [CG–SnO_2]$_{0.5}$–$SWCNT_{0.5}$, the cycling did not significantly modify the R_S and R_{CT}, as seen at Table 2. However, the [CG–SnO_2]$_{0.5}$–$SWCNT_{0.5}$ electrode impedance was higher than that of [CG–SnO_2]$_{0.0}$–$SWCNT_{1.0}$. One plausible explanation for this phenomenon is that the particles are larger in the [CG–SnO_2]$_{0.5}$–$SWCNT_{0.5}$ composite paper and consequently the electrode impedance is higher. As the particles are larger, the cross-sectional area for Li-ion intercalation per active mass is smaller. Then, the EIS spectra for [CG–SnO_2]$_{0.5}$–$SWCNT_{0.5}$ composite paper electrodes clearly reflect the multistep nature of the overall Li-ion insertion process. Aurbach [42] proposed that the semicircles at high and low frequency are relative to the porous part and the compact interphase, respectively. We assumed that the composite paper containing 0.5 wt% of ball-milled C–SnO_2 could have constituted a multilayer structure. Finally, after 30 cycles, the impedance of [CG–SnO_2]$_{0.5}$–$SWCNT_{0.5}$ composite paper remained higher than that of [CG–SnO_2]$_{0.0}$–$SWCNT_{1.0}$ and, consequently, the R_{CT} was higher as well. As commented before, there is a change in the volume of SnO_2 during the insertion/extraction of Li ions during cycling and consequently an increase in interparticle contact resistance. Then, the higher value of R_{CT} for [CG–SnO_2]$_{0.5}$–$SWCNT_{0.5}$ composite paper after 30 cycles compared to the [CG–SnO_2]$_{0.0}$–$SWCNT_{1.0}$ paper electrode can be attributed to the increase in the internal resistance of the electrode induced by the SEI film formation on the surface of particles of the active material during cycling [43].

Table 2 EIS estimated solution resistance (R_S) and charge–transfer resistance (R_{CT}) for [CG–SnO_2]$_{0.0}$–$SWCNT_{0.0}$ and for [CG–SnO_2]$_{0.5}$–$SWCNT_{0.5}$ at fresh cell and after 30 cycles of charge/discharge

Resistances (Ω cm^2)	[CG–SnO_2]$_{0.0}$–$SWCNT_{0.0}$		[CG–SnO_2]$_{0.5}$–$SWCNT_{0.5}$	
	Fresh cell	After 30 cycles	Fresh cell	After 30 cycles
R_S	2.0 ± 0.03	1.0 ± 0.04	12.2 ± 0.2	18.4 ± 0.9
R_{CT}	259 ± 3	96.4 ± 1.3	3130 ± 400	3620 ± 127

Conclusions

In summary, we have designed and fabricated CG–SnO_2–SWCNT as free-standing composite paper prepared by two-step process: ball-milling and vacuum filtration techniques. The galvanostatic test results indicate the $[CG–SnO_2]_{0.5}$–$SWCNT_{0.5}$ composite paper exhibits good electrochemical performance as anode material for lithium-ion batteries. A reversible capacity of 318 mA h g^{-1} could be retained at 0.08 mA cm^{-2} over 30 cycles. It also delivers a much-improved cycling performance compared to another SWCNT-based electrodes, 155 mA h g^{-1}. The best electrochemical performance of $[CG–SnO_2]_{0.5}$–$SWCNT_{0.5}$ composite paper was due to the content of the following: (i) CNTs, as flexible mechanical support with high electric conductivity, and (ii) SnO_2, as an active second phase to provide high capacity. The $[CG–SnO_2]_{0.5}$–$SWCNT_{0.5}$ composite paper is a promising lithium-ion battery anode material that does not need a current collector.

Acknowledgements The authors are grateful to Professors Hua Kun Liu, Jiazhao Wang and Shulei Chou of the University of Wollongong—Institute for Superconducting and Electronic Materials—for their assistance in this work. The authors thank the Laboratory of Structural Characterization (LCE/DEMa/UFSCar) for the general facilities and the Professor Valmor Mastelato for the XPS measures.

Funding information This study was financed in part by the Coordenação de Aperfeiçoamento de Pessoal de Nível Superior—Brasil (CAPES)—Finance Code 001 and by Conselho Nacional de Pesquisa e Desenvolvimento (CNPq, #167430/2017-3).

References

1. Tarascon JM, Armand M (2001) Nature 414(6861):359–367
2. Zubi G, Dufo-Lopez R, Carvalho M, Pasaoglu G (2018) Renew Sust Energ Rev 89:292–308
3. Du Y, Gao T, Ma W, Li H (2018) Chem Phys Lett 712:7–12
4. Golmohammadzadeh R, Faraji F, Rashchi F (2018) Resour Conserv Recycl 136:418–435
5. Castaneda LF, Walsh FC, Nava JL, de Leon CP (2017) Electrochim Acta 258:1115–1139
6. Kumar S, Nehra M, Kedia D, Dilbaghi N, Tankeshwar K, Kim KH (2018) Prog Energ Combust 64:219–253
7. Zhang D, Zhou Y, Liu CH, Fan SS (2016) Nanoscale 8(21):11161–11167
8. Montoro LA, Matsubara EY, Rosolen JM (2014) J Power Sources 257:205–212
9. Chew SY, Ng SH, Wang JZ, Novak P, Krumeich F, Chou SL, Chen J, Liu HK (2009) Carbon 47(13):2976–2983
10. Wang L, Wei Z, Mao M, Wang H, Li Y, Ma J (2019) Energy Storage Materials 16:434–454
11. Chou SL, Wang JZ, Zhong C, Rahman MM, Liu HK, Dou SX (2009) Electrochim Acta 54(28):7519–7524
12. Deng YF, Fang CC, Chen GH (2016) J Power Sources 304:81–101
13. Wang XY, Zhou XF, Yao K, Zhang JG, Liu ZP (2011) Carbon 49(1):133–139
14. Zhang CF, Peng X, Guo ZP, Cai CB, Chen ZX, Wexler D, Li S, Liu HK (2012) Carbon 50(5):1897–1903
15. Qin J, Zhao NQ, Shi CS, Liu EZ, He F, Ma LY, Li QY, Li JJ, He CN (2017) J Mater Chem A 5(22):10946–10956
16. Guo Q, Zheng Z, Gao HL, Ma J, Qin X (2013) J Power Sources 240:149–154
17. Wang MS, Wang ZQ, Yang ZL, Huang Y, Zheng JM, Li X (2017) Electrochim Acta 240:7–15
18. Ren J, Ren R-P, Lv Y-K (2018) Chem Eng J 353:419–424
19. Ng SH, Wang J, Guo ZP, Wang GX, Liu HK (2005) Electrochim Acta 51(1):23–28
20. Feng CQ, Li L, Guo ZP, Li H (2010) J Alloys Compd 504(2):457–461
21. Maheshwari PH, Nithya C, Jain S, Mathur RB (2013) Electrochim Acta 92:55–63
22. Saleh TA, Agarwal S, Gupta VK (2011) Applied Catalysis B 106:46–53
23. Liu RL, Chi YQ, Fang L, Tang ZS, Yi X (2014) J Nanosci Nanotechno 14(2):1647–1657
24. Zhang H, Chen K, He Y, Zhu Y, Chen Y, Wu C, Wang J, Liao JH, Liu SH (2001) J Phys Chem Solids 62(11):2007–2010
25. de la Chapelle ML, Stéphan C, Nguyen TP, Lefrant S, Journet C, Bernier P, Munoz E, Benito A, Maser WK, Martinez MT, de la Fuente GF, Guillard T, Flamant G, Alvarez L, Laplaze D (1999) Synth Met 103(1-3):2510–2512
26. Chipara DM, Macossay J, Ybarra AVR, Chipara AC, Eubanks TM, Chipara M (2013) Appl Surf Sci 275:23–27
27. Janas D, Stando G (2017) Sci Rep 7(1):12274
28. Zhang S, Yue L, Wang M, Feng Y, Li Z, Mi J (2018) Solid State Ionics 323:105–111
29. Kim JH, Choi SM, Nam SH, Seo MH, Choi SH, Kim WB (2008) Applied Catalysis B 82(1-2):89–102
30. Moulder JF, Stickle WF, Sobol PE, Bomben KD (1992) Handbook of X-ray photoelectron spectroscopy: a reference book of standard spectra for identification and interpretation of XPS data. Perkin-Elmer Corporation, Minnesota
31. Wang Z, Liang ZY, Wang B, Zhang C, Kramer L (2004) Composites Part A 35(10):1225–1232
32. Song HW, Li N, Cui H, Wang CX (2014) Electrochim Acta 120:46–51
33. Aurbach D, Koltypin M, Teller H (2002) Langmuir 18(23):9000–9009
34. Claye AS, Fischer JE, Huffman CB, Rinzler AG, Smalley RE (2000) J Electrochem Soc 147(8):2845–2852
35. Yuan L, Guo ZP, Konstantinov K, Wang JZ, Liu HK (2006) Electrochim Acta 51(18):3680–3684
36. Noerochim L, Wang JZ, Chou SL, Wexler D, Liu HK (2012) Carbon 50(3):1289–1297
37. Wang GX, Ahn JH, Lindsay MJ, Sun L, Bradhurst DH, Dou SX, Liu HK (2001) J Power Sources 97(8):211–215
38. Huang XK, Cui SM, Chang JB, Hallac PB, Fell CR, Luo YT, Metz B, Jiang JW, Hurley PT, Chen JH (2015) Angew Chem Int Edit 54(5):1490–1493
39. Cheng Y, Yi Z, Wang CL, Wu YM, Wang LM (2017) Chem Eng J 330:1035–1043
40. Frackowiak E, Gautier S, Gaucher H, Bonnamy S, Beguin F (1999) Carbon 37(1):61–69
41. Lee S, Cho D, Jeong Y (2015) Fiber Polym 16(7):1600–1604
42. Aurbach D (2000) J Power Sources 89(2):206–218
43. Guo ZP, Zhao ZW, Liu HK, Dou SX (2005) Carbon 43(7):1392–1399